

Realization of nodal-ring semimetal in pressurized black phosphorusKazuto Akiba ^{1,*}, Yuichi Akahama ², Masashi Tokunaga ³, and Tatsuo C. Kobayashi ¹¹Graduate School of Natural Science and Technology, Okayama University, Okayama 700-8530, Japan²Graduate School of Science, University of Hyogo, Kamigori, Hyogo 678-1297, Japan³The Institute for Solid State Physics, The University of Tokyo, Chiba 277-8581, Japan

(Received 8 February 2024; revised 27 March 2024; accepted 10 April 2024; published 3 May 2024)

Topological semimetals are intriguing targets for exploring unconventional physical properties of massless fermions. Among them, nodal-line or nodal-ring semimetals have attracted attention for their unique one-dimensional band contact in momentum space and resulting nontrivial quantum phenomena. By field angular resolved magnetotransport measurements and theoretical calculations, we show that pressurized black phosphorus (BP) is an ideal nodal-ring semimetal with weak spin-orbit coupling, which has a sole and carrier density-tunable nodal ring isolated from other trivial bands. We also revealed that the large magnetoresistance effect and its field-angular dependence in semimetallic BP are due to highly anisotropic relaxation time. Our results establish pressurized BP as an elemental model material for exploring nontrivial quantum properties unique to the topological nodal ring.

DOI: [10.1103/PhysRevB.109.L201103](https://doi.org/10.1103/PhysRevB.109.L201103)

Three-dimensional topological semimetals (TSMs) are a major research topic at the forefront of condensed matter physics [1]. A notable feature of TSMs is massless fermions in the bulk, which derive from the linearly dispersing band structure. Their unconventional physical properties due to the presence of massless fermions have been intensively explored and elucidated. Dirac and Weyl semimetals [2–8] are widely known materials that are characterized by degenerate or nondegenerate band contact points in the momentum space. Another type of TSM is a nodal-line or nodal-ring semimetal [9], in which the contact of the valence and conduction band occurs on a continuous line or closed ring in the momentum space. Numerous unique physical properties characterizing the nodal-line or nodal-ring semimetal are expected, including a drumheadlike flat surface state [10], unconventional distribution of Landau levels [11], nontrivial π -Berry phase associated with the band contact line [12], etc.

However, an ideal TSM is rarely seen in reality; other trivial carriers generally coexist, other than the massless fermions, which hinder the extraction of the true physical response derived from the topological electronic structure. In addition, the topological character is inherent in the crystal structure, constituent element, etc., which are difficult to desirably control from the outside.

In this context, we focus on black phosphorus (BP), which is known as a monoatomic semiconductor with a band gap of 0.3 eV at the Z point in the first Brillouin zone at ambient pressure [13–15]. The crystal structure has puckered honeycomb layers, which are alternately stacked along the b axis, as shown in the inset of Fig. 1(b) [16,17]. BP shows a pressure-induced semiconductor-to-semimetal transition at ~ 1.4 GPa [18–22]. In the semimetallic state, the

carrier density of electrons and holes can be continuously tuned by applying pressure, maintaining its compensated nature and high carrier mobility [23]. There have been several suggestions for the electronic structure in the semimetallic state [20,24–27], including the possible realization of topological nodal-line semimetal [28]. Intriguingly, several materials such as the nonmagnetic CaP₃ family [29,30] and magnetic EuP₃ [31], which share a similar puckered-layer structure with BP, have been focused on as candidates of nodal-ring semimetals. Experimentally, however, the Fermi surface (FS) in the semimetallic BP has been veiled so far primarily because of the lack of detailed geometry under high pressure.

In this study, we unveil the FS of semimetallic BP by angular resolved magnetotransport and show that pressurized BP is an ideal topological nodal-ring semimetal. Single crystals of BP were synthesized under high pressure [32,33], which show a high residual resistivity ratio of more than 400 at 3.4 GPa, as shown in the Supplemental Material [34]. The orthorhombic crystal structure ($Cmca$, space group No. 64) and the crystal orientation were determined by x-ray Laue backscattering image and simulations using QLaue [35]. The Laue pattern (see the Supplemental Material [34]) was reasonably explained by the lattice parameters determined by a recent neutron diffraction measurement [33]. Resistivity measurements under high pressures up to 3.5 GPa were performed using an indenter-type pressure cell [36] and Daphne oil 7474 pressure medium [37]. The pressure in the sample space was determined from the superconducting transition temperature of Pb set near the sample [38]. The band structure calculations based on the density-functional theory (DFT) and subsequent analyses were performed using the QUANTUM ESPRESSO [39–41], WANNI90 [42], WANNIERTOOLS [43,44], FERMISURFER [45], and SKEAF code [46]. In the following, we discuss the results based on scalar-relativistic calculations since the effect of the spin-orbit coupling is

* akb@okayama-u.ac.jp

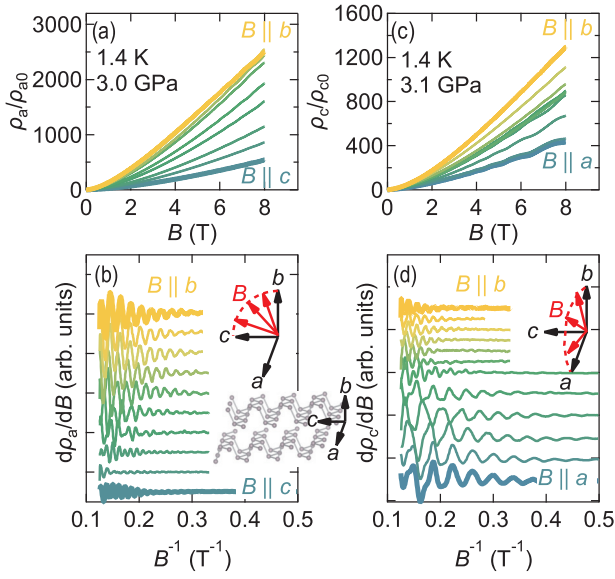


FIG. 1. (a) Magnetic field dependence of resistivity ρ_a normalized by zero-field value ρ_{a0} and (b) $d\rho_a/dB$ at 1.4 K and 3.0 GPa. B is rotated within the bc plane, and I is along the a axis. (c) Magnetic field dependence of resistivity ρ_c normalized by zero-field value ρ_{c0} and (d) $d\rho_c/dB$ at 1.4 K and 3.1 GPa. B is rotated within the ab plane, and I is along the c axis. Data in (b) and (d) are vertically shifted for clarity. The crystal structure of BP and its crystal axes are shown in the insets of (b).

negligibly small. A more detailed description of the experimental and theoretical methods are shown in the Supplemental Material [34].

First, we focus on the magnetotransport properties and their field angular dependence in the semimetallic state. Figure 1(a) shows the magnetic field (B) dependence of ρ_a at 1.4 K and 3.0 GPa, which is normalized by the zero-field value ρ_{a0} . Here, we rotated B within the bc plane. The current (I) direction is perpendicular to B . We observed a large magnetoresistance (MR) effect, which was maximized by the application of B along the b axis. To extract the SdH oscillations on such a large MR, we show $d\rho_a/dB$ as a function of B^{-1} in Fig. 1(b). We can see clear SdH oscillations and their variations according to the field direction. In Figs. 1(c) and 1(d), we show the resistivity along the c axis normalized by the zero-field value (ρ_c/ρ_{c0}) at 1.4 K and 3.1 GPa, in which B was rotated within the ab plane. In this configuration, we also observed a large MR effect maximized by the application of $B \parallel b$, and prominent SdH oscillations.

By collecting the field angular resolved SdH oscillations at various pressures, we can obtain the detailed geometry and pressure-induced evolution of the FS. Figures 2(a)–2(f) show the field angular dependence of the SdH frequency (F) obtained by fast Fourier transform (FFT) analysis at three representative pressures. The FFT spectra used to construct Figs. 2(a)–2(f) are shown in the Supplemental Material [34]. Although the datasets shown in (a), (c), (e) and (b), (d), (f) are obtained using different setups and samples, we can observe reasonable reproducibility of F at approximately the same pressure. At all pressures, we identified two independent branches labeled α and β with eye guides. Here, we can see

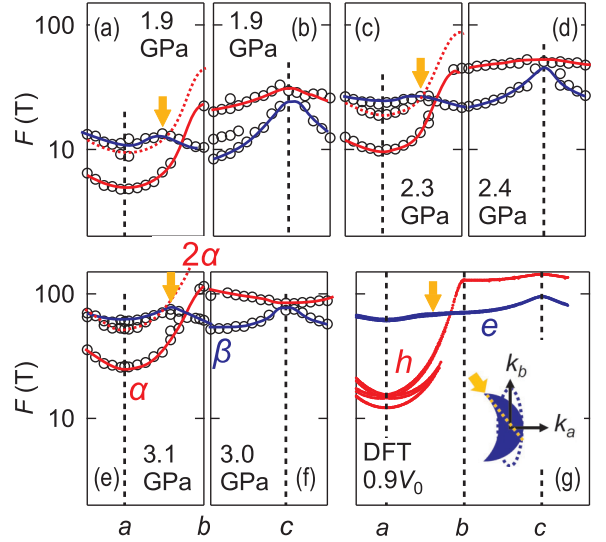


FIG. 2. Field angular dependence of the SdH frequency F at (a), (b) 1.9 GPa, (c), (d) 2.3–2.4 GPa, and (e), (f) 3.0–3.1 GPa. Identified branches (α , β) and second harmonics (2α) are shown with solid and broken eye guides, respectively. (g) Field angular dependence of F obtained from DFT calculation. The inset in (g) represents possible deformation of the electron pocket from the perfect ellipsoid, which can cause local maxima between a and b , as indicated by arrows.

another frequency around $B \parallel a$, which lies just below the β . We confirmed at all pressures that these are second harmonics of α . The observation of 2α is consistent with our previous study [20]. We can see that F of α and β monotonically increases with the application of pressure with little change in their angular dependencies. The monotonic increase of F corresponds to the increase in the carrier density indicated by the two-carrier model analyses [23]. Here, we can recognize a pressure-induced change in the angular dependence of α between $B \parallel b$ and $B \parallel c$, which will be discussed later. From the above results, we can conclude there exist two independent Fermi pockets and no other FSs appear at least up to 3.0–3.1 GPa.

To determine the FS of the semimetallic BP, we performed first-principles calculations. The black curve in Fig. 3(a) shows the band structure of BP at ambient pressure using a fully optimized structure, which reproduces the direct band gap structure at the Z point. Here, $V_0 = 171.0 \text{ \AA}^3$ in Fig. 3(a) represents the volume of the unit cell obtained by structural optimization, and the Fermi level is taken at the top of the valence band. The band structure at ambient pressure is consistent with a previous report [47]. The red curve in Fig. 3(a) shows the band structure of compressed BP with a volume of $0.9 V_0$. The result was obtained using a crystal structure optimized under hydrostatic compression, and the Fermi level was adjusted to satisfy the carrier compensation. For details of structural optimization; see the Supplemental Material [34]. As seen at the Z point, the valence and conduction band touch at a point near the Fermi level. Although the conduction band significantly falls toward the Fermi level on the Γ - A path, the present result indicates that the emergence of the FS initially occurs at the Z point. This picture is qualitatively different from those suggested in several previous reports [20,25], in

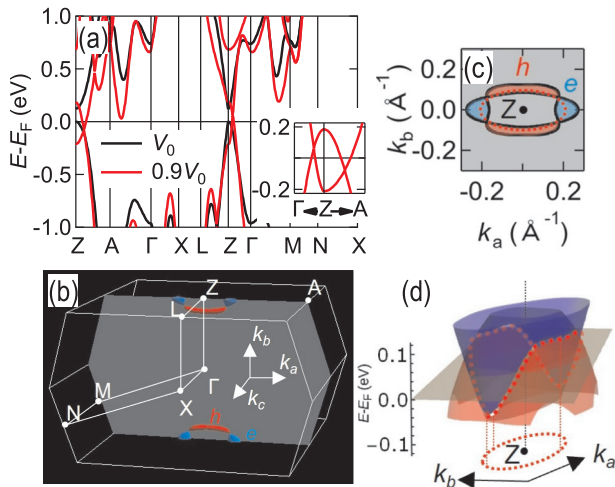


FIG. 3. (a) Energy band structure under ambient (black) and compressed (red) conditions. V_0 represents the volume of the optimized structure at ambient pressure (see text for details). The inset shows a magnified view of the band dispersion at the Z point. (b) FS under compressed conditions. The red and blue surfaces represent the hole and electron pockets, respectively. (c) Cross section of the FS cut by the k_a - k_b plane. The red broken line indicates the projection of the nodal ring on the k_a - k_b plane. (d) Dispersion of the valence (red surface) and conduction (blue surface) bands on the k_a - k_b plane. Red broken lines represent the nodal ring enclosing the Z point.

which four additional electron pockets exist on the Γ -A path. A possible reason for this difference might account for the computational details and whether the structure was optimized or not.

Figure 3(b) shows the FS drawn in the first Brillouin zone. We obtained an elongated banana-shaped hole (h) pocket and a relatively isotropic electron (e) pocket. As shown in Fig. 3(c), these pockets touch at four nodes and enclose the Z point in the k_a - k_b plane. To deepen our understanding of the obtained FS, we show in Fig. 3(d) the dispersion of the valence and conduction bands on the k_a - k_b plane. As indicated by the red broken line, the band-touching point mentioned in Fig. 3(a) forms a closed ring structure in the k_a - k_b plane. This nodal ring does not lie exactly on the Fermi level but shows a slight dispersion of $\pm \sim 100$ meV around the Fermi level. This results in a squeezed ring-shaped FS formed by h and e pockets. The above results predict the realization of a nodal-ring semimetal, in which there only exists a set of FSs deriving from the nodal-ring structure. The above discussion can hardly be affected by whether spin-orbit coupling is included or not, as shown in the Supplemental Material [34]. This indicates that BP under pressure is a unique platform possessing an ideal nodal ring located within $\pm \sim 100$ meV around the Fermi level.

Then, we confirm the realization of the predicted FS. Figure 2(g) shows the field angular dependence of F calculated based on the obtained FS. As expected from the banana-shaped geometry, h pocket shows a steep angular dependence between a and b . The e pocket shows rather flat dependence with local maximum and minimum at c and a , respectively. A comparison with Figs. 2(e) and 2(f) shows that the experimental features in the angular dependence and absolute

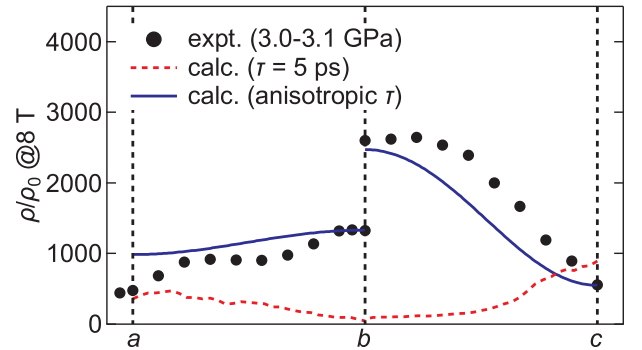


FIG. 4. (a) Field angular dependence of the MR effect at 8 T with $I \perp B$. The markers represent the experimental results. The red broken and blue solid lines represent the calculation results assuming a constant relaxation time $\tau = 5$ ps and anisotropic τ , respectively (see main text).

value of F are satisfactorily reproduced by our calculation, demonstrating the realization of the nodal-ring semimetal.

In both the experimental and theoretical results, we can recognize a local maxima between a and b indicated by the arrows in Fig. 2. Qualitatively, these can be understood assuming that the poles of an ellipsoidal FS deviate from k_b , as illustrated in the inset of Fig. 2(g). This structure corresponds to the pointy contacts directed along the nodal ring suggested by the DFT results shown in Figs. 3(b) and 3(c). From the position of the local maxima, we determined that the tangent line of the nodal ring at the contact point of h and e pockets directs $45^\circ - 55^\circ$ from k_b .

Here, we also note in Figs. 2(a)–2(f) that the field angular dependence of α between $B \parallel b$ and $B \parallel c$ apparently changes by application of pressure. At 1.9 GPa, the h pocket is assumed to be slightly flat on the k_a - k_b plane, which results in a larger cross section when $B \parallel c$. At 3.0–3.1 GPa, on the other hand, the FS becomes flat on the k_c - k_a plane as can be seen in the larger F when $B \parallel b$. We show the schematic images of the expected geometry in the Supplemental Material [34] to help understand the situation. The above change of flat direction is assumed to continuously take place by the application of pressure. This delicate change resolved in our experiment could not be reproduced by the simulation, presumably due to the potential difficulty to evaluate a tiny Fermi surface with high accuracy in the first-principles calculations.

Next, we attempt to understand the large MR effect characterizing the semimetallic state. First, we focus on the transport properties arising from the FS curvature. We theoretically evaluated the MR effect based on the semiclassical Boltzmann equation, whose result is shown by the red broken line in Fig. 4 (for details, see the Supplemental Material [34]). Here, we assume that the relaxation time $\tau = 5$ ps is independent of the band indices and directions. Apparently, the calculation fails to reproduce the magnitude and field angular dependence of the MR observed in the experiments.

This mismatch is assumed to be derived from the constant- τ approximation. To consider the possible band-index dependence and anisotropy of τ , we adopt a model in which the mobility tensor of h and e pockets $\hat{\mu}^{h,e}$ and the

magnetic tensor \hat{B} are given by [48]

$$\hat{\mu}^{h,e} = e \begin{pmatrix} \tau_{xx}^{h,e}/m_{xx}^{h,e} & 0 & 0 \\ 0 & \tau_{yy}^{h,e}/m_{yy}^{h,e} & 0 \\ 0 & 0 & \tau_{zz}^{h,e}/m_{zz}^{h,e} \end{pmatrix}, \quad (1)$$

$$\hat{B} = \begin{pmatrix} 0 & -B_z & B_y \\ B_z & 0 & -B_x \\ -B_y & B_x & 0 \end{pmatrix}. \quad (2)$$

Here, x , y , and z correspond to a , c , and b directions, respectively. In this framework, the geometry of the FS is approximated to an ellipsoid characterized by the effective mass tensor $\hat{m}^{h,e}$. On the other hand, we can treat τ as a pocket- and direction-dependent tensor $\hat{\tau}^{h,e}$. The conductivity tensor $\hat{\sigma}$ and resistivity tensor $\hat{\rho}$ can be given by $\hat{\sigma} = 2[n_h e(\hat{\mu}^h + \hat{B})^{-1} + n_e e(\hat{\mu}^e - \hat{B})^{-1}]$ and $\hat{\rho} = \hat{\sigma}^{-1}$. To reproduce the experimental data at 3.0–3.1 GPa, shown by the markers in Fig. 4, we calculated the resistivity normalized by the zero-field value by adjusting the six parameters in $\hat{\mu}^{h,e}$. A reasonable reproduction was achieved as indicated by the solid lines in Fig. 4, in which $\mu_{xx}^h = 1.5 \text{ T}^{-1}$, $\mu_{yy}^h = 10 \text{ T}^{-1}$, and $\mu_{zz}^h = 12 \text{ T}^{-1}$ for h , and $\mu_{xx}^e = 8 \text{ T}^{-1}$, $\mu_{yy}^e = 8 \text{ T}^{-1}$, and $\mu_{zz}^e = 1 \text{ T}^{-1}$ for e . Here, we assumed a slight carrier imbalance, $n_h = 3.05 \times 10^{18} \text{ cm}^{-3}$ and $n_e = 3.00 \times 10^{18} \text{ cm}^{-3}$ for each pocket, to reflect the positive Hall resistivity in the high-field region [23]. In fact, this model reasonably reproduces the experimental features of Hall resistivity, including the sign inversion in the low-field region (see the Supplemental Material [34]). Thus, the above parameters depict a minimal model for expressing the transport properties of semimetallic BP.

Since the geometry of the FS has been established by first-principles calculations, we can calculate the cyclotron effective mass m_c of each pocket when B is applied along the three principal axes. The results are $m_c^{B||a}/m_0 = 0.0476$, $m_c^{B||b}/m_0 = 0.302$, and $m_c^{B||c}/m_0 = 0.318$ for h , and $m_c^{B||a}/m_0 = 0.106$, $m_c^{B||b}/m_0 = 0.151$, and $m_c^{B||c}/m_0 = 0.171$ for e , where m_0 represents the bare mass of electron. These show reasonable agreement with the experimental value, $m_c/m_0 = 0.02 - 0.14$ [20,21]. Thus, we can evaluate $\hat{m}^{h,e}$ as $m_{xx}^h/m_0 = 2.02$, $m_{yy}^h/m_0 = 0.0453$, and $m_{zz}^h/m_0 = 0.0500$ for h , and $m_{xx}^e/m_0 = 0.244$, $m_{yy}^e/m_0 = 0.0936$, and $m_{zz}^e/m_0 = 0.121$ for e . Here, we assumed relationships $m_c^{B||x} = \sqrt{m_{yy}m_{zz}}$, etc. Combining the above $\hat{m}^{h,e}$ with the experimentally deduced $\hat{\mu}^{h,e}$, we can extract the relaxation time in ps as

$$\hat{\tau}^h = \begin{pmatrix} 17.2 & 0 & 0 \\ 0 & 2.58 & 0 \\ 0 & 0 & 3.41 \end{pmatrix}, \quad \hat{\tau}^e = \begin{pmatrix} 11.1 & 0 & 0 \\ 0 & 4.26 & 0 \\ 0 & 0 & 0.685 \end{pmatrix}. \quad (3)$$

The above result reveals that τ strongly depends on the direction and type of pocket, which is the reason for the failure of the constant- τ approximation. Notably, anisotropic $\hat{\mu}^e$ is crucial to explain the large MR effect and its field angular dependence. Because the relatively isotropic geometry of the e pocket is validated by both experiments and calculations, the significant anisotropy of $\hat{\mu}^e$ is primarily responsible for $\hat{\tau}^e$.

The phonon is almost inactive at 1.4 K; thus, carrier-defect or carrier-carrier scattering may be responsible for the anisotropic $\hat{\tau}^{h,e}$. Although the specific mechanism is unclear at this stage, we would like to comment on possible causes.

One is the anisotropic crystal structure of BP. The a direction having the longest τ for both h and e corresponds to the direction along the grooves of the puckered layer. Thus, it might be preferable for ballistic transport compared to the buckled and layered directions. We also note that the compressibility of BP is strongly direction dependent. As shown in a previous report [33], the lattice constant along the a axis is hardly affected by the application of pressure, implying fewer defects accompanied by lattice compression.

Another one is unconventional the scattering process, which is theoretically predicted in nodal-ring semimetals. In particular, FS accompanied by a nodal ring can bring a two-dimensional weak antilocalization (2D WAL) effect assuming a long-range impurity potential [49,50]. In this case, the backscattering process, which dictates the electrical resistivity, is dominated by an interference loop confined in a specific plane perpendicular to the nodal line. The longer $\hat{\tau}_{xx}^{h,e}$ may involve protection from backscattering under the presence of the 2D WAL effect. It has been suggested that a high aspect ratio between the radius of the nodal ring (K_0) and the poloidal radius of the FS (κ) in momentum space is favorable for the emergence of the 2D WAL effect [30,50]. Based on $K_0 \sim 0.15 \text{ \AA}^{-1}$ and $\kappa \sim 0.036 \text{ \AA}^{-1}$ obtained from the computational result shown in Fig. 3, $K_0/\kappa \sim 4.2$ can be estimated for BP at around 3 GPa. Here, K_0 is estimated as an averaged value of the long and short axes of the oval nodal ring, and κ is calculated using an average of extremal cross sections of h and e pockets. We would like to point out that this is comparable to the case of SrAs₃ ($K_0/\kappa \sim 3.3$ – 4.5) [30], which has a torus-shaped FS with a high K_0/κ ratio and shows a 2D WAL effect. To reinforce the above nontrivial mechanism, further detailed and systematic inspection of electrical conductivity in the semimetallic state would be necessary, which remains a future challenge.

In summary, we have unveiled the Fermi surface (FS) in semimetallic black phosphorus (BP) by magnetotransport measurements. We identified two independent FSs in the semimetallic state above 1.4 GPa, and no other FSs were detected up to 3.0–3.1 GPa. Our theoretical calculation suggested the emergence of the FS at the Z point in the first Brillouin zone and the realization of the nodal-ring structure enclosing the Z point. The nodal ring has an energy dispersion of $\pm \sim 100 \text{ meV}$ around the Fermi level, which results in a squeezed ring-shaped FS consisting of small hole and electron pockets. Because of the weak spin-orbit coupling of phosphorus, the gap at the band contact node is quite small. The simulated angular dependence of the Shubnikov-de Haas oscillations satisfactorily reproduced the experimental features, which clarified the realization of the nodal-ring semimetal. We also demonstrated that anisotropic relaxation time is crucial for reproducing the large magnetoresistance effect and its field angular dependence in semimetallic BP. Importantly, the semimetallic BP has the sole nodal ring isolated from other trivial bands, and the figure of the nodal ring and carrier density can be flexibly tuned by pressure. Our results have established the realization of an ideal nodal-ring semimetal in

pressurized BP, which can be a promising platform to systematically explore novel phenomena derived from the nontrivial electronic structure.

We thank Y. Fuseya, H. Sakai, Y. Seo, and S. Araki for the valuable discussion. This study was supported by JSPS KAKENHI Grants No. 22K14006 and No. 23H04862.

- [1] B. Q. Lv, T. Qian, and H. Ding, Experimental perspective on three-dimensional topological semimetals, *Rev. Mod. Phys.* **93**, 025002 (2021).
- [2] A. A. Burkov and L. Balents, Weyl semimetal in a topological insulator multilayer, *Phys. Rev. Lett.* **107**, 127205 (2011).
- [3] Z. Wang, H. Weng, Q. Wu, X. Dai, and Z. Fang, Three-dimensional Dirac semimetal and quantum transport in Cd_3As_2 , *Phys. Rev. B* **88**, 125427 (2013).
- [4] Z. K. Liu, B. Zhou, Y. Zhang, Z. J. Wang, H. M. Weng, D. Prabhakaran, S.-K. Mo, Z. X. Shen, Z. Fang, X. Dai, Z. Hussain, and Y. L. Chen, Discovery of a three-dimensional topological Dirac semimetal, Na_3Bi , *Science* **343**, 864 (2014).
- [5] Z. K. Liu, J. Jiang, B. Zhou, Z. J. Wang, Y. Zhang, H. M. Weng, D. Prabhakaran, S.-K. Mo, H. Peng, P. Dudin, T. Kim, M. Hoesch, Z. Fang, X. Dai, Z. X. Shen, D. L. Feng, Z. Hussain, and Y. L. Chen, A stable three-dimensional topological Dirac semimetal Cd_3As_2 , *Nat. Mater.* **13**, 677 (2014).
- [6] S.-Y. Xu, I. Belopolski, N. Alidoust, M. Neupane, G. Bian, C. Zhang, R. Sankar, G. Chang, Z. Yuan, C.-C. Lee, S.-M. Huang, H. Zheng, J. Ma, D. S. Sanchez, B. Wang, A. Bansil, F. Chou, P. P. Shibayev, H. Lin, S. Jia, and M. Z. Hasan, Discovery of a Weyl fermion semimetal and topological Fermi arcs, *Science* **349**, 613 (2015).
- [7] Y. Wu, D. Mou, N. H. Jo, K. Sun, L. Huang, S. L. Bud'ko, P. C. Canfield, and A. Kaminski, Observation of Fermi arcs in the type-II Weyl semimetal candidate WTe_2 , *Phys. Rev. B* **94**, 121113(R) (2016).
- [8] K. Deng, G. Wan, P. Deng, K. Zhang, S. Ding, E. Wang, M. Yan, H. Huang, H. Zhang, Z. Xu, J. Denlinger, A. Fedorov, H. Yang, W. Duan, H. Yao, Y. Wu, S. Fan, H. Zhang, X. Chen, and S. Zhou, Experimental observation of topological Fermi arcs in type-II Weyl semimetal MoTe_2 , *Nat. Phys.* **12**, 1105 (2016).
- [9] A. A. Burkov, M. D. Hook, and L. Balents, Topological nodal semimetals, *Phys. Rev. B* **84**, 235126 (2011).
- [10] Y. Kim, B. J. Wieder, C. L. Kane, and A. M. Rappe, Dirac line nodes in inversion-symmetric crystals, *Phys. Rev. Lett.* **115**, 036806 (2015).
- [11] J.-W. Rhim and Y. B. Kim, Landau level quantization and almost flat modes in three-dimensional semimetals with nodal ring spectra, *Phys. Rev. B* **92**, 045126 (2015).
- [12] C. Li, C. M. Wang, B. Wan, X. Wan, H.-Z. Lu, and X. C. Xie, Rules for phase shifts of quantum oscillations in topological nodal-line semimetals, *Phys. Rev. Lett.* **120**, 146602 (2018).
- [13] Y. Takao, H. Asahina, and A. Morita, Electronic structure of black phosphorus in tight binding approach, *J. Phys. Soc. Jpn.* **50**, 3362 (1981).
- [14] H. Ashahina, K. Shindo, and A. Morita, Electronic structure of black phosphorus in self-consistent pseudopotential approach, *J. Phys. Soc. Jpn.* **51**, 1193 (1982).
- [15] Y. Akahama, S. Endo, and S. Narita, Electrical properties of black phosphorus single crystals, *J. Phys. Soc. Jpn.* **52**, 2148 (1983).
- [16] R. Hultgren, N. S. Gingrich, and B. E. Warren, The atomic distribution in red and black phosphorus and the crystal structure of black phosphorus, *J. Chem. Phys.* **3**, 351 (1935).
- [17] A. Brown and S. Rundqvist, Refinement of the crystal structure of black phosphorus, *Acta Cryst.* **19**, 684 (1965).
- [18] Y. Akahama, S. Endo, and S. Narita, Electrical properties of single-crystal black phosphorus under pressure, *Physica B+C* **139-140**, 397 (1986).
- [19] Y. Akahama and H. Kawamura, Optical and electrical studies on band-overlapped metallization of the narrow-gap semiconductor black phosphorus with layered structure, *Phys. Status Solidi B* **223**, 349 (2001).
- [20] K. Akiba, A. Miyake, Y. Akahama, K. Matsubayashi, Y. Uwatoko, H. Arai, Y. Fuseya, and M. Tokunaga, Anomalous quantum transport properties in semimetallic black phosphorus, *J. Phys. Soc. Jpn.* **84**, 073708 (2015).
- [21] Z. J. Xiang, G. J. Ye, C. Shang, B. Lei, N. Z. Wang, K. S. Yang, D. Y. Liu, F. B. Meng, X. G. Luo, L. J. Zou, Z. Sun, Y. Zhang, and X. H. Chen, Pressure-induced electronic transition in black phosphorus, *Phys. Rev. Lett.* **115**, 186403 (2015).
- [22] T. Fujii, Y. Nakai, Y. Akahama, K. Ueda, and T. Mito, Pressure-induced evolution of band structure in black phosphorus studied by ^{31}P NMR, *Phys. Rev. B* **101**, 161408(R) (2020).
- [23] K. Akiba, A. Miyake, Y. Akahama, K. Matsubayashi, Y. Uwatoko, and M. Tokunaga, Two-carrier analyses of the transport properties of black phosphorus under pressure, *Phys. Rev. B* **95**, 115126 (2017).
- [24] R. Fei, V. Tran, and L. Yang, Topologically protected Dirac cones in compressed bulk black phosphorus, *Phys. Rev. B* **91**, 195319 (2015).
- [25] P.-L. Gong, D.-Y. Liu, K.-S. Yang, Z.-J. Xiang, X.-H. Chen, Z. Zeng, S.-Q. Shen, and L.-J. Zou, Hydrostatic pressure induced three-dimensional Dirac semimetal in black phosphorus, *Phys. Rev. B* **93**, 195434 (2016).
- [26] C.-H. Li, Y.-J. Long, L.-X. Zhao, L. Shan, Z.-A. Ren, J.-Z. Zhao, H.-M. Weng, X. Dai, Z. Fang, C. Ren, and G.-F. Chen, Pressure-induced topological phase transitions and strongly anisotropic magnetoresistance in bulk black phosphorus, *Phys. Rev. B* **95**, 125417 (2017).
- [27] T. Fujii, Y. Nakai, M. Hirata, Y. Hasegawa, Y. Akahama, K. Ueda, and T. Mito, Giant density of states enhancement driven by a zero-mode Landau level in semimetallic black phosphorus under pressure, *Phys. Rev. Lett.* **130**, 076401 (2023).
- [28] J. Zhao, R. Yu, H. Weng, and Z. Fang, Topological node-line semimetal in compressed black phosphorus, *Phys. Rev. B* **94**, 195104 (2016).
- [29] Q. Xu, R. Yu, Z. Fang, X. Dai, and H. Weng, Topological nodal line semimetals in the CaP_3 family of materials, *Phys. Rev. B* **95**, 045136 (2017).
- [30] H. Kim, J. Ok, S. Cha, B. Jang, C. Kwon, Y. Kohama, K. Kindo, W. Cho, E. Choi, Y. Jo, W. Kang, J. Shim, K. Kim, and J. Kim,

- Quantum transport evidence of isolated topological nodal-line fermions, *Nat. Commun.* **13**, 7188 (2022).
- [31] A. H. Mayo, H. Takahashi, M. S. Bahramy, A. Nomoto, H. Sakai, and S. Ishiwata, Magnetic generation and switching of topological quantum phases in a trivial semimetal α -EuP₃, *Phys. Rev. X* **12**, 011033 (2022).
- [32] S. Endo, Y. Akahama, S. Terada, and S. Narita, Growth of large single crystals of black phosphorus under high pressure, *Jpn. J. Appl. Phys.* **21**, L482 (1982).
- [33] Y. Akahama, M. Miyakawa, T. Taniguchi, A. Sano-Furukawa, S. Machida, and T. Hattori, Structure refinement of black phosphorus under high pressure, *J. Chem. Phys.* **153**, 014704 (2020).
- [34] See Supplemental Material at <http://link.aps.org/supplemental/10.1103/PhysRevB.109.L201103> for detailed information on the experimental and theoretical methods, and Hall resistivity calculated based on the ellipsoidal Fermi surface model.
- [35] <https://sourceforge.net/projects/qlaue/>
- [36] T. C. Kobayashi, H. Hidaka, H. Kotegawa, K. Fujiwara, and M. I. Eremets, Nonmagnetic indenter-type high-pressure cell for magnetic measurements, *Rev. Sci. Instrum.* **78**, 023909 (2007).
- [37] K. Murata, K. Yokogawa, H. Yoshino, S. Klotz, P. Munsch, A. Irizawa, M. Nishiyama, K. Iizuka, T. Nanba, T. Okada, Y. Shiraga, and S. Aoyama, Pressure transmitting medium Daphne 7474 solidifying at 3.7 GPa at room temperature, *Rev. Sci. Instrum.* **79**, 085101 (2008).
- [38] A. Eiling and J. S. Schilling, Pressure and temperature dependence of electrical resistivity of Pb and Sn from 1-300 K and 0-10 GPa-use as continuous resistive pressure monitor accurate over wide temperature range; superconductivity under pressure in Pb, Sn and In, *J. Phys. F: Met. Phys.* **11**, 623 (1981).
- [39] P. Giannozzi, S. Baroni, N. Bonini, M. Calandra, R. Car, C. Cavazzoni, D. Ceresoli, G. L. Chiarotti, M. Cococcioni, I. Dabo, A. D. Corso, S. de Gironcoli, S. Fabris, G. Fratesi, R. Gebauer, U. Gerstmann, C. Gougoussis, A. Kokalj, M. Lazzeri, L. Martin-Samos *et al.*, QUANTUM ESPRESSO: a modular and open-source software project for quantum simulations of materials, *J. Phys.: Condens. Matter* **21**, 395502 (2009).
- [40] P. Giannozzi, O. Andreussi, T. Brumme, O. Bunau, M. Buongiorno Nardelli, M. Calandra, R. Car, C. Cavazzoni, D. Ceresoli, M. Cococcioni, N. Colonna, I. Carnimeo, A. Dal Corso, S. De Gironcoli, P. Delugas, R. Distasio, A. Ferretti, A. Floris, G. Fratesi, G. Fugallo *et al.*, Advanced capabilities for materials modelling with QUANTUM ESPRESSO, *J. Phys.: Condens. Matter* **29**, 465901 (2017).
- [41] P. Giannozzi, O. Baseggio, P. Bonfà, D. Brunato, R. Car, I. Carnimeo, C. Cavazzoni, S. de Gironcoli, P. Delugas, F. Ferrari Ruffino, A. Ferretti, N. Marzari, I. Timrov, A. Urru, and S. Baroni, QUANTUM ESPRESSO toward the exascale, *J. Chem. Phys.* **152**, 154105 (2020).
- [42] G. Pizzi, V. Vitale, R. Arita, S. Bluegel, F. Freimuth, G. Géranton, M. Gibertini, D. Gresch, C. Johnson, T. Koretsune, J. Ibanez, H. Lee, J.-M. Lihm, D. Marchand, A. Marrazzo, Y. Mokrousov, J. I. Mustafa, Y. Nohara, Y. Nomura, L. Paulatto *et al.*, WANNIER90 as a community code: new features and applications, *J. Phys.: Condens. Matter* **32**, 165902 (2020).
- [43] Q. Wu, S. Zhang, H.-F. Song, M. Troyer, and A. A. Soluyanov, WANNIERTOOLS: An open-source software package for novel topological materials, *Comput. Phys. Commun.* **224**, 405 (2018).
- [44] S. N. Zhang, Q. S. Wu, Y. Liu, and O. V. Yazyev, Magnetoresistance from Fermi surface topology, *Phys. Rev. B* **99**, 035142 (2019).
- [45] M. Kawamura, FermiSurfer: Fermi-surface viewer providing multiple representation schemes, *Comput. Phys. Commun.* **239**, 197 (2019).
- [46] P. Rourke and S. Julian, Numerical extraction of de Haas-van Alphen frequencies from calculated band energies, *Comput. Phys. Commun.* **183**, 324 (2012).
- [47] J. Qiao, X. Kong, Z. Hu, F. Yang, and W. Ji, High-mobility transport anisotropy and linear dichroism in few-layer black phosphorus, *Nat. Commun.* **5**, 4475 (2014).
- [48] Y. Mitani and Y. Fuseya, Large longitudinal magnetoresistance of multivalley systems, *J. Phys.: Condens. Matter* **32**, 345802 (2020).
- [49] S. V. Syzranov and B. Skinner, Electron transport in nodal-line semimetals, *Phys. Rev. B* **96**, 161105(R) (2017).
- [50] W. Chen, H.-Z. Lu, and O. Zilberberg, Weak localization and antilocalization in nodal-line semimetals: dimensionality and topological effects, *Phys. Rev. Lett.* **122**, 196603 (2019).